Author/s:
Chung, D;Monty, JP;Hutchins, N

Title:
Similarity and structure of wall turbulence with lateral wall shear stress variations

Date:
2018-07-25

Citation:
Chung, D., Monty, J. P. & Hutchins, N. (2018). Similarity and structure of wall turbulence with lateral wall shear stress variations. Journal of Fluid Mechanics, 847, pp.591-613. https://doi.org/10.1017/jfm.2018.336.

Persistent Link:
https://hdl.handle.net/11343/252853

Similarity and structure of wall turbulence with lateral wall shear stress variations

D. Chung†, J. P. Monty and N. Hutchins

Department of Mechanical Engineering, University of Melbourne, Victoria 3010, Australia

(Received xx; revised xx; accepted xx)

Wall-bounded turbulence, where it occurs in engineering or nature, is commonly subjected to spatial variations in wall shear stress. A prime example is spatially varying roughness. Here, we investigate the configuration where the wall shear stress varies only in the lateral direction. The investigation is idealised in order to focus on one aspect, namely, the similarity and structure of turbulent inertial motion over an imposed scale of stress variation. To this end, we analyse data from direct numerical simulation (DNS) of pressure-driven turbulent flow through a channel bounded by walls of laterally alternating patches of high and low wall shear stress. The wall shear stress is imposed as a Neumann boundary condition such that the wall shear stress ratio is fixed at 3 while the lateral spacing s of the uniform-stress patches is varied from 0.39 to 6.28 of the half-channel height δ. We find that global outer-layer similarity is maintained when s is less than about 0.39δ while local outer-layer similarity is recovered when s is greater than about 6.28δ. However, the transition between the two regimes through $s \approx \delta$ is not monotonic owing to the presence of secondary roll motions that extend across the whole cross section of the flow. Importantly, these secondary roll motions are associated with an amplified skin-friction coefficient relative to both the small- and large-s/δ limits. It is found that the relationship between the secondary roll motions and the mean isovels is reversed through this transition from low longitudinal velocity over low stress at small s/δ to high longitudinal velocity over low stress at large s/δ.

Key words: turbulent boundary layers, turbulent flows, turbulence simulation

1. Introduction

Wall-bounded turbulence rarely flows over spatially uniform roughness. Applications abound where roughness, and hence the wall shear stress, varies spatially, with examples including barnacle clusters on ship hulls, rivet rows on aircraft and wind-turbine arrays in wind farms. Loosely speaking, spatially varying roughness is characterised by statistical variations of roughness elements occurring over wall-parallel scales that are comparable or exceed the large scales of wall turbulence. In contrast, spatially uniform roughness is characterised by length scales that are all smaller than the large scales of wall turbulence. Although there currently exist well-established scaling laws that underpin textbook methods such as the Moody chart (Moody 1944) for predicting turbulent flows over spatially uniform roughness, the same cannot be said of spatially varying roughness. Predictions for the spatially varying regime can be obtained by extrapolating from the spatially uniform regime but this comes at the cost of uncertainties that are currently

† Email address for correspondence: daniel.chung@unimelb.edu.au

not well quantified, with even the delineation between the two regimes currently not well appreciated. The present investigation is an attempt to address these issues as well as to shed light on the general changes to the similarity and structure of rough-wall turbulence from the spatially uniform through to the spatially varying regime. This is achieved by analysing direct numerical simulation (DNS) data of turbulent flow through a channel bounded by walls idealised with laterally varying roughness whereby the scale of roughness variation can be systematically varied while secondary or non-essential parameters are respectively fixed, minimised or eliminated.

1.1. *Idealisation of spatially varying roughness*

Progress in understanding specific complex turbulent boundary layer flows is often aided by reducing the problem into a set of canonical configurations and drawing general conclusions about a broader class of turbulent flows. In distilling the wider problem of spatially varying roughness, two issues need to be tackled: first is the representation of the roughness and second is the choice of the spatial variation. In the following, we discuss the rationale of our present treatment of these issues.

The first issue is the representation of roughness. As far as the turbulent inertial motions in the log and outer layers are concerned, classical understanding of wall turbulence dictates that the only relevant parameters are the wall shear stress τ_0 and the outer scale δ, which, for the present flow, is equal to the half-channel height. The turbulent inertial motion disregards whether the wall is smooth or rough and, for a rough wall in particular, the roughness height k does not play a direct role even though it sets τ_0. This is of course the outer-layer similarity hypothesis of Townsend (1976), which is based upon dimensional considerations and backed by evidence overwhelmingly in its favour (Flack & Schultz 2014). Further, in an idealised simulation in which k is entirely eliminated by directly imposing a uniform τ_0 as boundary condition, we previously showed that turbulent inertial motions are essentially similar in the log and outer layers (Chung *et al.* 2014). In light of this classical understanding, if the purpose is to study the impact of spatial variations of roughness on turbulent inertial motions, then extending the idealised simulations of Chung *et al.* (2014) by imposing spatial variations directly on τ_0 and circumventing k appears to be a sensible approach. Imposing spatial variations directly on τ_0 comes at the cost of not knowing how k sets τ_0 but this issue is perhaps better addressed in research pertaining to spatially uniform roughness, where the preoccupation has been and continues to be the mapping between the geometric parameter k to the dynamic parameter k_s that leads to τ_0 for any given roughness (e.g. Raupach *et al.* 1991; Jiménez 2004; Flack & Schultz 2014). Imposing spatial variations directly on τ_0 comes with the benefit of low blockage by roughness, that is, small k/δ. Since the imposed stresses are viscous, the roughness sublayer k is replaced by the viscous sublayer $10\nu/u_\tau$, where ν is the kinematic viscosity and $u_\tau \equiv (\tau_0/\rho)^{1/2}$, the friction velocity. As such, the blockage is small but finite, $(10\nu/u_\tau)/\delta = 10/\delta^+$. The requirement of low blockage, often numerically quoted as $k/\delta \lesssim 1/40$ (Jiménez 2004), is necessary in order to distinguish between flow over roughness proper, in which a log layer remains intact and therefore generalisable to other wall-bounded flows, versus flow over obstacles, in which a log layer is absent and therefore specific to a particular outer-flow geometry. The low-blockage requirement is often prohibitively expensive for simulations that resolve roughness elements but the choice of idealisation here ensures that the simulations remain relevant to the roughness regime as opposed to the obstacle regime while manageable with regards to computational cost, thereby enabling us to perform our intended parametric investigation. The directly imposed variation on τ_0 also avoids issues related to changes to the dynamic origin, or step, which typically accompanies a variation in the roughness height.

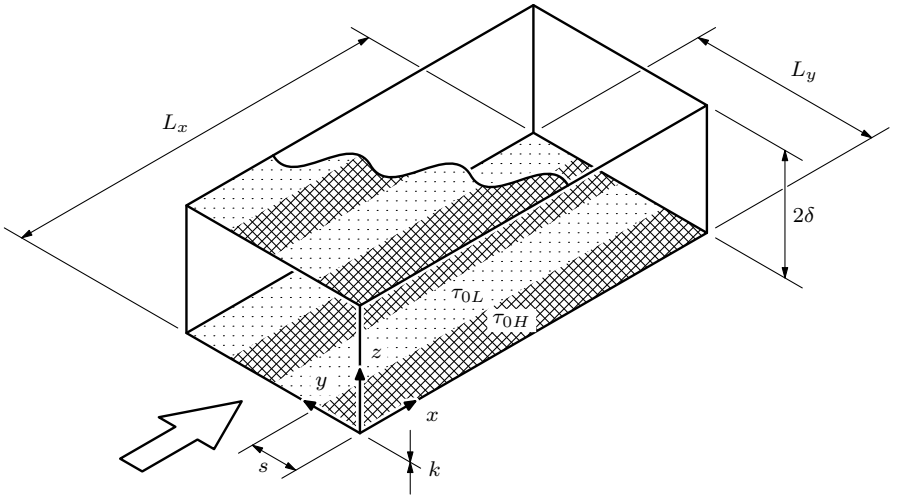

FIGURE 1. Setup of idealised DNS to investigate the effect of lateral wall shear stress variations. The width of each uniform-stress patch is $s = s_H = s_L$. The stress pattern at the top wall (partially shown) is simply the reflection, across the channel centreline, of the bottom wall. The streamwise wall shear stresses is low in dotted regions labelled τ_{0L} and high in the hatched regions labelled τ_{0H}.

The second issue is the choice of the spatial variation of roughness (wall shear stress). Spatial variations in roughness can and do occur in any number of ways. A useful classification has been to restrict the variation to occur in only one direction at a time. Within this classification are two configurations that have been the subject of previous research: longitudinally (streamwise-) varying roughness and laterally (spanwise-) varying roughness. We will here focus on laterally varying roughness, and specifically, square-wave variations, that is, patches of laterally alternating otherwise-uniform high or low wall shear stress, respectively τ_{0H} and τ_{0L} (figure 1). Apart from being simple, uniform-stress patches are fairly common, arising from man-made or natural boundaries. Two parameters need to be further specified, namely, the wall shear stress ratio τ_{0H}/τ_{0L}, and the lateral size of high and low uniform-stress patches, s_H and s_L. Here we fix $\tau_{0H}/\tau_{0L} = 3$, $s_H = s_L = s$ and systematically increase s from 0.39δ to 6.28δ in multiples of 2. This parametric sweep would cover the cases where the turbulent inertial motions, which scale with δ, are larger and smaller than the imposed scale s.

The Reynolds number is selected to be as high as feasible, presently set at $Re_\tau \equiv u_{\overline{\tau}}\delta/\nu = 590$, where $u_{\overline{\tau}}$, $\equiv (\overline{\tau}_0/\rho)^{1/2}$, the friction velocity based on the wall shear stress averaged across the whole channel $\overline{\tau}_0$, which, in turn, can be related to τ_{0H} and τ_{0L} for $s_H = s_L$ via $\overline{\tau}_0 = (\tau_{0H} + \tau_{0L})/2$. That is, $\tau_{0H} = (3/2)\overline{\tau}_0$ and $\tau_{0L} = (1/2)\overline{\tau}_0$. For reference, suppose for the moment that τ_{0L} and τ_{0H} were, respectively, the wall shear stresses of smooth- and rough-wall turbulent channel flows with matched δ, ν and $U(\delta)$, where $U(\delta)$ is the mean centreline velocity. Then $\tau_{0H}/\tau_{0L} = 3$ implies an equivalent roughness Reynolds number k_s^+ for the rough-wall flow that we now estimate as follows. Recall that $U(\delta)$ can be expressed as

$$\frac{U(\delta)}{u_{\tau L}} = \frac{1}{\kappa}\log\Big(\frac{\delta u_{\tau L}}{\nu}\Big) + A \quad \text{and} \quad \frac{U(\delta)}{u_{\tau H}} = \frac{1}{\kappa}\log\Big(\frac{\delta u_{\tau H}}{\nu}\Big) + A - \Delta U^+ \quad (1.1a,b)$$

for the smooth and rough walls, respectively. The outer wake contribution has been neglected, which is a reasonable approximation for turbulent channel flows;

$u_{\tau L} \equiv (\tau_{0L}/\rho)^{1/2}$ and $u_{\tau H} \equiv (\tau_{0H}/\rho)^{1/2}$, respectively, the smooth- and rough-wall friction velocities; $\kappa \approx 0.4$, the von Kármán constant; $A \approx 5.1$, the smooth-wall intercept and ΔU^+ is the Hama roughness function (cf. Jiménez 2004). Subtracting the rough profile (1.1*b*) from the smooth profile (1.1*a*) gives $\Delta U^+ = [U(\delta)/u_{\tau L}][1 - (u_{\tau L}/u_{\tau H})] - (1/\kappa)\log(u_{\tau L}/u_{\tau H})$. Then, substituting $u_{\tau L}/u_{\tau H} = (\tau_{0L}/\tau_{0H})^{1/2} = (1/3)^{1/2}$ and $U(\delta)/u_{\tau L} \approx 20.2$, obtained from the smooth-wall profile (1.1*a*) with $\delta u_{\tau L}/\nu = (u_{\tau L}/u_{\overline{\tau}})(\delta u_{\overline{\tau}}/\nu) = (1/2)^{1/2}(590) \approx 417$, gives $\Delta U^+ \approx 9.9$. Alternatively, using $\Delta U^+ = (1/\kappa)\log k_s^+ + A - 8.5$ (cf. Jiménez 2004), we obtain $k_s^+ \approx 205$. That is, the hypothetical rough-wall flow is in the fully rough regime.

There are other ways to perform the study more realistically. However, we consider the hyper-simplication a strength. We have idealised the boundary conditions to seek generalisations for the outer-flow behaviour, independent of whether stress variations are caused by roughness or topography or other effects.

1.2. *Brief review of previous research on laterally varying roughness*

Laterally varying roughness is generally associated with stress-induced secondary roll motions (Hinze 1967, 1973; Townsend 1976; Bradshaw 1987; Nugroho *et al.* 2013; Willingham *et al.* 2014; Barros & Christensen 2014; Jelly *et al.* 2014; Anderson *et al.* 2015; Vanderwel & Ganapathisubramani 2015), which physically distinguishes and separates its study from longitudinally varying roughness, the latter associated with growing internal layers (Antonia & Luxton 1971, 1972; Bou-Zeid *et al.* 2004; Saito & Pullin 2014; Hanson & Ganapathisubramani 2016). An enduring prediction in the area is for the direction of secondary flow, due to Hinze (1967). By simplifying the turbulent kinetic energy equation, Hinze (1967) predicted that upwelling secondary flow occurs where dissipation exceeds production of turbulent kinetic energy, coinciding with low shear stress regions and, conversely, downwelling secondary flow occurs where production exceeds dissipation of turbulent kinetic energy, coinciding with high shear stress regions. The link between the high dissipation relative to production for low shear stress and vice versa was made on empirical grounds (Hinze 1973). The overall prediction of secondary flow received further detailed corroboration by the large-eddy simulation (LES) study of Anderson *et al.* (2015). However, a question that pertains to the relationship between (time-averaged) isovels and secondary flow remains unresolved, namely, whether high or low longitudinal velocities (relative to the spanwise average at a given wall-normal location), the so-called high- or low-momentum pathways (Barros & Christensen 2014), occur over low shear stress. (The same question can be posed for high shear stress.) Intuitively, one may expect to find high longitudinal velocities over low shear stress given the lower resistance but the LES data of Willingham *et al.* (2014) show that precisely the opposite situation occurs. In fact, Hinze (1973) mentions in passing that both could occur, but did not elaborate on the conditions that preferred one situation over the other. On the other hand, the experiment of Vanderwel & Ganapathisubramani (2015) that systematically varies the lateral spacing between roughness elements S from $S/\delta \approx 0.30$ to 1.76 reports that low longitudinal velocities always occur over roughness elements, suggesting that only one of the isovel–secondary-flow relationships is preferred. Further, the dynamic-origin effect cannot be discounted as an important factor in the aforementioned experiment, as seen in the isolated riblets of Goldstein & Tuan (1998). The present investigation lends further insights into such questions pertaining to the structure of secondary flow with the help of high-fidelity DNS data comprising small and large s/δ cases while fixing, minimising or eliminating other parameters. The focus of the present paper is on the effect of lateral variations of τ_0, however these variations are generated.

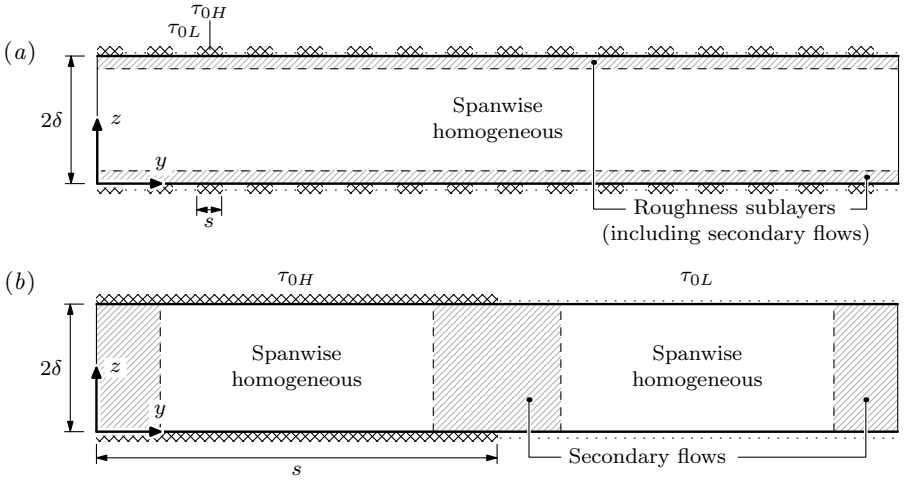

FIGURE 2. Cross section of channel, illustrating the flow structure of the (a) spatially uniform, $s \ll \delta$, and (b) spatially varying, $s \gg \delta$, regimes. The longitudinal (x-direction) flow is out of the page.

1.3. *Delineation between spatially varying and spatially uniform roughness regimes*

The degree of roughness uniformity must be measured against the inherent scales of the turbulent motion that flows over it. That is, roughness uniformity, like the degree of roughness height, is a dynamic property of the flow. How a particular roughness 'feels' to the flow is quantitatively expressed through statistics of turbulent relative motion such as velocity differences or fluctuations (which are invariant to Galilean transformations). Consider, for instance, how the flow expresses itself through the global mean velocity defect $\overline{U}(\delta) - \overline{U}(z)$ at a given wall distance z over roughness. The appropriate flow scales are the outer-layer thickness δ, the distance from the wall z and the viscous wall unit ν/u_τ. For the roughness, the number of characteristic scales could be infinite, but for our idealised laterally varying roughness (figure 1), the only scale to consider is s. The intention is for the roughness idealisation to be a model that isolates the influence of the largest lateral length scale of a given roughness, which could be the integral length scale for unordered roughness or the wavelength of the largest repeating unit for ordered roughness. For such a flow characterised by this list of flow and roughness scales, the general form for the global mean velocity defect that pertains to the bulk of the flow can thus be written as

$$\frac{\overline{U}(\delta) - \overline{U}(z)}{u_\tau} = \Phi\left(\frac{z}{\delta}, \frac{z}{\nu/u_\tau}, \frac{z}{s}, \frac{\tau_{0H}}{\tau_{0L}}\right). \tag{1.2}$$

In order to obtain outer-layer similarity as hypothesised by Townsend (1976), then both $\nu/u_\tau \ll z$ and $s \ll z$, whence a finite τ_{0H}/τ_{0L} is also irrelevant, so that

$$\frac{\overline{U}(\delta) - \overline{U}(z)}{u_\tau} = f\left(\frac{z}{\delta}\right). \tag{1.3}$$

This form is impervious to the details of the bounding wall and is universal for a given outer-flow geometry. In other words, the wall shear stress u_τ appears to be spatially uniform to the turbulent inertial motion that, scaling with δ, dominate the dynamics in the bulk of the flow. In this dynamical sense, the roughness is said to be spatially uniform (figure 2a). This regime is characterised by the two inequalities leading to (1.3). The first inequality requires the wall location z to be far above the influence of viscosity,

classically taken to be $30\nu/u_\tau < z$ (Tennekes & Lumley 1972), above the buffer layer. This is essentially the high Reynolds number requirement and is well understood. The second inequality requires the wall location z to be sufficiently far above the inhomogeneous layer of the flow that is influenced by roughness, called the roughness sublayer or the blending height, the latter used in the context of spatially varying roughness (e.g. Bou-Zeid *et al.* 2007). That is, above the blending height, the local defect, $U(y,\delta) - U(y,z)$, for all y locations are identical. The requirement in terms of s is less familiar but the version in terms of k is often quoted as 2–3$k < z$ (Jiménez 2004) and $5k < z$ (Flack *et al.* 2007), depending on the specific roughness geometry. The present idealisation in figure 1 highlights the point that a lateral scale of roughness can be important in its own right, especially for low-aspect-ratio ($k/s \ll 1$) roughness. Combining $s \ll z$ with the implicit $z < \delta$, the spatially uniform regime can be delineated as $s \ll \delta$, see figure 2(a). This regime is realised, for example, in superhydrophic surfaces (Jelly *et al.* 2014).

When $s \approx \delta$ or $\delta \ll s$, similarity of the global defect can no longer be expected. However, similarity of the local defect with the local shear stress can arise under certain conditions. To see this, consider now the local mean velocity defect $U(y,\delta) - U(y,z)$ at wall distance z and lateral station y relative to a high-to-low stress jump located at y_0. Dimensional considerations lead to the following general form,

$$\frac{U(y,\delta) - U(y,z)}{u_\tau(y)} = \phi\left(\frac{y-y_0}{\delta}, \frac{z}{\delta}, \frac{z}{\nu/u_\tau(y)}, \frac{s}{\delta}, \frac{\tau_{0H}}{\tau_{0L}}\right), \tag{1.4}$$

where $u_\tau(y)$ is $u_{\tau H} \equiv (\tau_{0H}/\rho)^{1/2}$ for $y < y_0$ and $u_{\tau L} \equiv (\tau_{0L}/\rho)^{1/2}$ for $y > y_0$. If $s \approx \delta$, this full list of parameters must be retained. However, if $\delta \ll s$ so that stations y exist that are several outer-layer thicknesses δ away from a stress jump, i.e. $\delta \ll |y - y_0|$, the local mean velocity defect is expected to take on the same one-dimensional outer-layer form f as (1.3),

$$\frac{U_H(\delta) - U_H(z)}{u_{\tau H}} = \frac{U_L(\delta) - U_L(z)}{u_{\tau L}} = f\left(\frac{z}{\delta}\right), \tag{1.5}$$

where $U_H(\delta) - U_H(z) = [U(\delta,y) - U(z,y)]_{\delta \ll |y-y_0|}$ for $y < y_0$ (high shear stress) and $U_L(\delta) - U_L(z) = [U(\delta,y) - U(z,y)]_{\delta \ll |y-y_0|}$ for $y > y_0$ (low shear stress). In this limit, the turbulent inertial motion above the buffer layer ($\nu/u_\tau(y) \ll z$) deep within a uniform stress patch ($\delta \ll |y - y_0| < s$) 'does not know' about the flow in neighbouring patches characterised by different values of wall shear stresses. This dynamical behaviour that occurs when $\delta \ll s$ invites the label, spatially varying roughness, see figure 2(b).

The orders of the constants for the inequalities that characterise the spatially uniform and spatially varying regimes, $s \ll \delta$ and $\delta \ll s$, could depend on τ_{0H}/τ_{0L}. Some insights into this dependence will be obtained from the present DNS data. The adherence of flow behaviour to either of these limiting regimes can be quantified by collapse in either the global defect (1.3) or local defect (1.5).

2. DNS setup

The channel-flow setup is shown in figure 1. The wall-normal direction is z, with walls located at $z = 0$ and $z = 2\delta$. Periodic boundary conditions are imposed in the streamwise (x) and spanwise (y) directions. Alternating high and low wall shear stresses, τ_{0H} and τ_{0L} respectively, are imposed uniformly within each patch of width s at the walls using the shear stress (Neumann) boundary condition, $\nu(\partial u/\partial z)_{z=0} = \tau_{0H}/\rho$ or τ_{0L}/ρ at the bottom wall and $-\nu(\partial u/\partial z)_{z=2\delta} = \tau_{0H}/\rho$ or τ_{0L}/ρ at the top wall. The no-slip boundary condition is not satisfied. As stated in §1, this boundary condition is

Boundary condition	s/δ	τ_{0H}/τ_{0L}	δ_H^+	δ_L^+	N_x	N_y	N_z	L_y/δ	Δ_{xH}^+	Δ_{yH}^+	Δ_{zcH}^+	Tu_τ/δ
No slip	$\cdots$	Uniform		$\cdots$	384	384	256	3.14	9.7	4.8	7.2	52
Shear stress	$\cdots$	Uniform		$\cdots$	512	512	384	3.14	7.2	3.6	4.8	56
Shear stress	0.39	3	723	417	512	512	384	3.14	8.9	4.4	5.9	57
Shear stress	0.79	3	723	417	512	512	384	3.14	8.9	4.4	5.9	56
Shear stress	1.57	3	723	417	512	512	384	3.14	8.9	4.4	5.9	54
Shear stress	3.14	3	723	417	512	1024	384	6.28	8.9	4.4	5.9	54
Shear stress	6.28	3	723	417	512	2048	384	12.57	8.9	4.4	5.9	55

TABLE 1. Simulation parameters. $Re_\tau \equiv u_\tau \delta/\nu$; $u_\tau \equiv (\overline{\tau}_0/\rho)^{1/2}$; $\overline{\tau}_0 \equiv (\tau_{0H} + \tau_{0L})/2$, the average wall shear stress; $s_H = s_L = s$, the patch width (figure 1); superscript '+' indicates viscous scaling with either $u_{\tau H}/\nu$ for subscript 'H' or $u_{\tau L}/\nu$ for subscript 'L', e.g. $\delta_H^+ = \delta u_{\tau H}/\nu$; and T is the duration of statistics collection after initial transients are discarded. $Re_\tau = 590$ and $L_x/\delta \approx 6.28$ for all present simulations.

meant to represent an idealised roughness with low roughness blockage (k/δ small) and without changes to the dynamic origin. This boundary condition imparts no additional length scales on the flow other than the wall unit, ν/u_τ, and its spatial variation. The stress pattern is mirrored across the channel centreline and spanwise wall shear stress is zero uniformly, $\nu(\partial v/\partial z)_{z=0,2\delta} = 0$. Note that these idealised piecewise-uniform boundary conditions do not account for variations in wall shear stress that typically occur near stress jumps in real flows due to localised secondary flow. We confirmed, in a simulation where $(v)_{z=0,2\delta} = 0$ for the case $s/\delta \approx 1.57$, that the outer relative motions are virtually indistinguishable between the free-slip and no-slip v boundary conditions. The impermeable boundary condition $w_{z=0,2\delta} = 0$ is enforced uniformly at both the walls. The uniform shear-stress boundary condition was previously compared with the usual no-slip boundary condition at matched Re_τ, the main finding there being that the flows above the buffer layers, $z^+ \approx 30$, are essentially similar (Chung *et al.* 2014). This includes means, Reynolds stresses, spectrograms and higher-order moments. Whilst the outer region obeys similarity, the inner region is impacted by the choice of boundary conditions, as expected. In particular, Chung *et al.* (2014) showed, for the synthetic uniform wall shear stress (Neumann) boundary condition, that the streamwise normal Reynolds stress peaks at the wall rather than away from the wall (their figure 2*a*) and that the viscous sublayer is neither linear nor logarithmic but a shifted log law still appears above $z^+ \approx 30$ (their figure 1*b*). This number agrees with classical estimates (Tennekes & Lumley 1972) and gives an indication to the lower bound below which the present flow is sensitive and therefore specific to the way in which the wall shear stress is applied. Above the buffer layer, the present flow is expected to behave similarly to other flows with the same spatially varying wall shear stress. Data from the reference no-slip and uniform shear stress cases (first two rows of table 1) will be included where relevant to aid in interpreting the statistics at hand. The wall shear stress boundary condition, in combination with the Navier–Stokes equations, are impervious to arbitrary Galilean transformations in the wall-parallel plane. In practice, a frame of reference must be chosen; here, it is chosen such that the bulk wall-parallel velocity is zero, which reduces numerical dispersion errors (Bernardini *et al.* 2013). It is important to only refer to Galilean-invariant statistics such as velocity differences or fluctuations, which are unambiguous and unaffected by the arbitrary frame of reference of the present simulations.

A parametric sweep for $s/\delta \approx 0.39$–6.28 is performed at the matched friction Reynolds

number, $Re_\tau \equiv u_{\overline{\tau}}\delta/\nu = 590$, where the friction velocity $u_{\overline{\tau}}$ is based on the average wall shear stress $\overline{\tau}_0 \equiv (\tau_{0H} + \tau_{0L})/2$. The stress ratio is fixed $\tau_{0H}/\tau_{0L} = 3$ for the cases here with stress variations. The simulations are well resolved, set by the wall unit of the high shear stress patch where the finest scales are expected to be smaller, $\Delta_x < 8.9\nu/u_{\tau H}$, $\Delta_y < 4.4\nu/u_{\tau H}$ and $\Delta_{zc} < 5.9\nu/u_{\tau H}$, where Δ_{zc} is the largest wall-normal cell spacing at the channel centre (cf. Moser *et al.* 1999). The wall-normal cells are stretched with a cosine mapping. The CFL number, defined here as $\Delta_t \max\{|u|/\Delta_x, |v|/\Delta_y, |w|/\Delta_z\}$ is fixed to unity, where Δ_t is the time step size. Statistics are collected over many eddy-turnover times, $T \gtrsim 50\delta/u_{\overline{\tau}}$. Unlike simulations that are statistically homogeneous in the wall-parallel plane, the plane average that offers a quicker convergence cannot be used here and so the longer averaging times are required in order to obtain x-averaged statistics at each (y, z) location. The length of the channel domain for all simulations is 6.28δ, which is just large enough (cf. Moser *et al.* 1999; Lozano-Durán & Jiménez 2014); the width of the channel domain is 3.14δ for $s \lesssim 1.57\delta$, but increased up to 12.57δ for $s \approx 6.28\delta$ in order to accommodate at least one period of high and low stress patch. This choice constrains the flow to scales narrower than $L_y/\delta \approx 3.14$, 6.28 and 12.57, for the cases, $s/\delta \approx 1.57$, 3.14 and 6.28, respectively, ruling out motions wider than L_y, which may be important if large-scale phenomena, such as meandering, is of interest. Nonetheless, we expect minimal influence to scales narrower than 3.14δ, which are captured in all the present simulations, and the domain width is sufficient (Lozano-Durán & Jiménez 2014) for mean statistics reported herein to be robust.

Here, DNS is performed using the fourth-order symmetry-preserving spatial discretisation of Verstappen & Veldman (2003), along with the boundary conditions of Sanderse *et al.* (2014). This spatial discretisation conserves mass, momentum and energy on a staggered grid. The semi-implicit low-storage third-order Runge–Kutta–Wray scheme (Spalart *et al.* 1991) marches the equations in time and the fractional-step method (e.g. Perot 1993) projects the intermediate velocity onto a divergence-free space. The viscous terms are treated implicitly only in the wall-normal direction (involving the inversion of a heptadiagonal matrix). This present code is written by the first author and has been used in a number of previous DNS studies of wall-bounded flows (e.g. Chung *et al.* 2014; Kozul *et al.* 2016).

3. Results and discussion

3.1. *Global mean longitudinal velocity defect*

First, we look for indications of the spatially uniform regime by considering the spanwise-averaged or 'global' longitudinal (streamwise) velocity defect, shown in figure 3. Recall that the roughness or wall shear stress can be considered spatially uniform from a dynamical point of view if the global velocity defect collapses according to (1.3). The profiles for the no-slip and uniform shear stress boundary condition cases are also shown in figure 3, indicating collapse above the buffer layer, $z^+ \gtrsim 30$, as previously demonstrated by Chung *et al.* (2014). This suggests that differences below this location should be considered specific to the boundary-condition treatment. Above this location, the uniform shear stress case serves as a reference such that departures away from it can be interpreted as a flow modification that is attributed to laterally varying roughness. Consider now the cases with imposed spatially varying wall shear stress. The global defect of the $s/\delta \approx 0.39$ case is virtually indistinguishable from the uniform shear-stress case, suggesting that this case is in the spatially uniform regime. Increasing s/δ to 0.79 breaks outer-layer similarity such that the flow departs from the spatially uniform regime. This

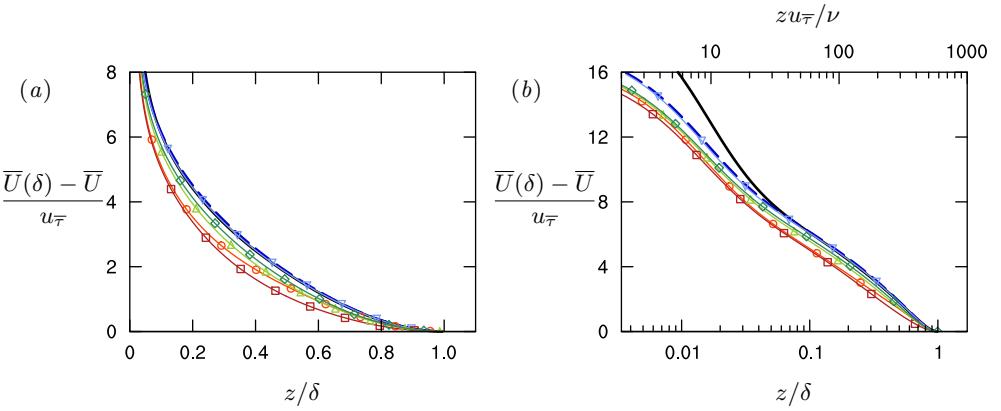

FIGURE 3. Global mean (spanwise-avaraged) velocity defect in (a) linear–linear and (b) log–linear coordinates: ——, no slip; – –, uniform stress; —▽—, $s/\delta = 0.39$; —○—, $s/\delta = 0.79$; —□—, $s/\delta = 1.57$; —△—, $s/\delta = 3.14$; —◇—, $s/\delta = 6.28$.

departure is an abrupt drop in the velocity defect through the bulk of the flow, with an approximate vertical shift in the logarithmic region seen in figure 3(b). However, this reduction in velocity defect is not monotonic. For $s/\delta \approx 0.79$–1.57, the global defect reduces to a flatter profile before appearing to revert back towards the spatially uniform regime for $s/\delta \approx 3.14$–6.28.

The reduction of the global defect to a flatter profile has been reported in a similar context in the experiment of Vanderwel & Ganapathisubramani (2015) at $Re_\tau \approx 4200 \pm 400$. There the flow is a boundary layer over streamwise-aligned protrusions, where the lateral spacing S between the protrusions of width $\mathcal{W}$ is varied from $S/\delta \approx 0.30$ to 1.76 at fixed $\mathcal{W}/\delta \approx 0.15$. They identify two behaviours: 'fine' spacing for $S/\delta \approx 0.30$–0.45, where the global defects collapse, and 'coarse' spacing for $S/\delta \approx 0.88$–1.76, where the global defects appear to also collapse, but are flatter relative to the 'fine' spacing cases, see their figure 3(a). The present DNS data is quantitatively consistent with these experiments with s equivalent to S. The spatially uniform regime collapses the present $s/\delta \approx 0.39$, no-slip and uniform shear stress cases, which can be identified with the 'fine' spacing cases of Vanderwel & Ganapathisubramani (2015). Also, the present $s/\delta \approx 0.79$, 1.57 cases have flatter profiles, which is similar to the 'coarse' spacing cases of Vanderwel & Ganapathisubramani (2015) except that the present $s/\delta \approx 0.79$, 1.57 profiles do not collapse. Even so, the overwhelming similarities suggest, but does not prove, the generalisation that the flow transitions away from the spatially uniform regime somewhere between $s/\delta \approx 0.39$–0.79 regardless of whether the flow is through a channel or a boundary layer, and independent of Reynolds number as the experiments are conducted at friction Reynolds numbers that are an order of magnitude larger than the present DNS. Further, the consistency in flow behaviour between a real experiment and the modelled boundary conditions supports the utility of the present idealised simulations for understanding flow over laterally varying roughness. Although the experiment of Vanderwel & Ganapathisubramani (2015) did not consider spacings S greater than 1.76δ, the present DNS data goes further to include two additional cases at $s/\delta \approx 3.14$, 6.28, showing that the global defect appears to revert back towards the spatially uniform regime. The reasons for this peculiar non-monotonic behaviour will be made clear in the following sections.

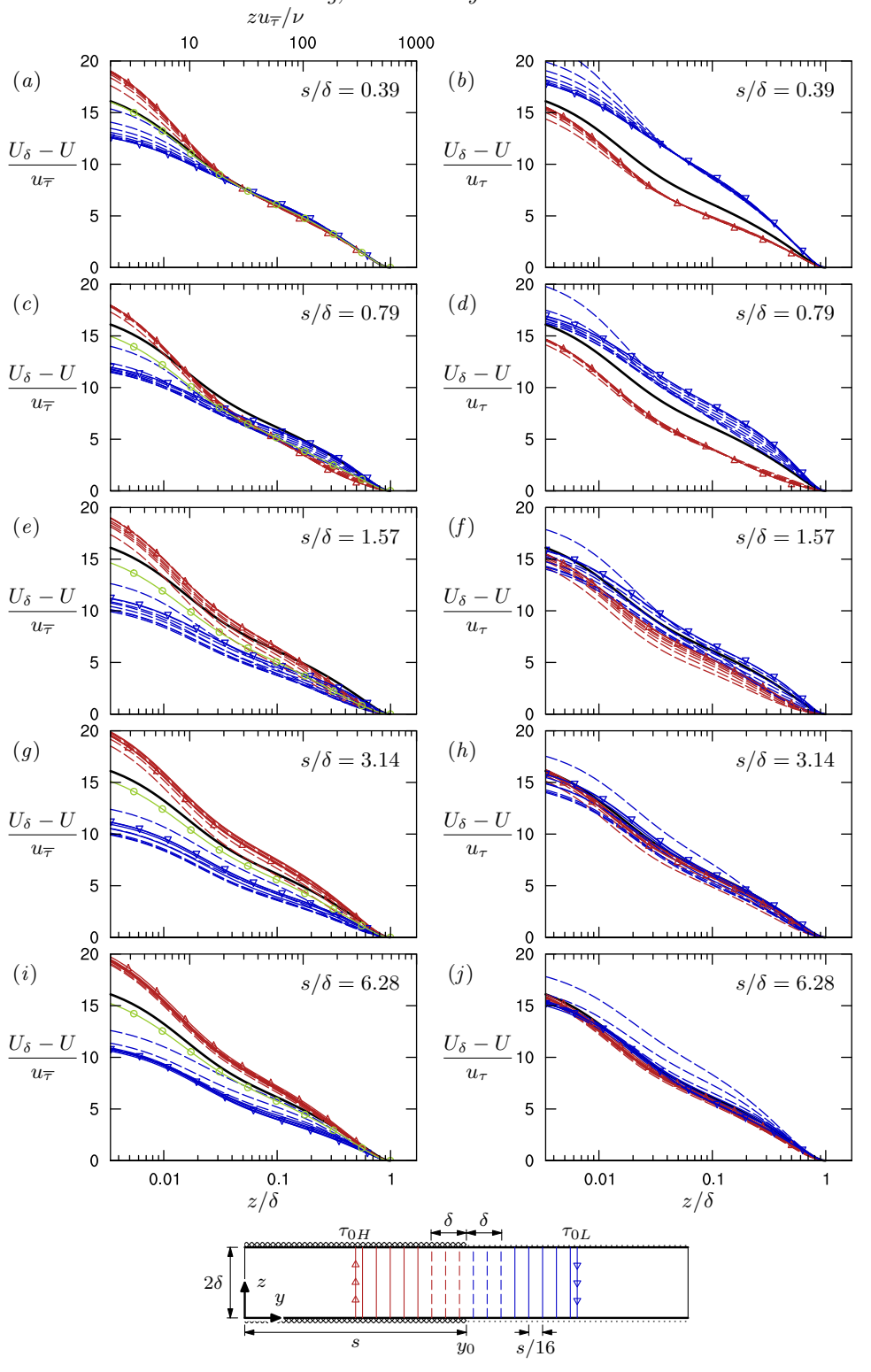

FIGURE 4. Local defect $U_\delta - U \equiv U(y,\delta) - U(y,z)$ at various lateral (y) stations: scaled with the averaged friction velocity u_τ, left panels, i.e. (a, c, e, g, i); scaled with the local friction velocity $u_\tau = u_{\tau H}$ or $u_{\tau L}$, right panels, i.e. (b, d, f, h, j). Top to bottom, $s/\delta \approx 0.39$, 0.79, 1.57, 3.14, 6.28; —, uniform shear stress; —△—, centre of high shear stress region; —▽—, centre of low shear stress region; —○—, global defect; ——, y in high shear stress region, dashed if within δ of stress jump; ——, y in low shear stress region, dashed if within δ of stress jump. See key at bottom.

3.2. *Local mean longitudinal velocity defect*

We now consider the local mean longitudinal velocity defect. In figure 4, the local defects at y stations located at the centres of the high shear stress regions, at the centres of the low shear stress regions and at 16 evenly spaced locations between the two centres are shown, see key at the bottom of figure 4. For reference, the uniform shear stress defect and the globally averaged defect (left panels only) are also shown. The y stations that are within δ of a stress jump y_0, i.e. $|y - y_0| < \delta$, are indicated by thin dashed lines without markers, while stations such that $|y - y_0| > \delta$ are indicated by thin solid lines without markers.

The left panels of figure 4 are scaled with the globally averaged friction velocity $u_{\overline{\tau}}$, that is, they are scaled in the same way as figure 3, but access to the local defects at various y stations provide more detail of the structural changes to the flow. The plots in the left panels corroborate the dimensional intuition discussed in § 1.3 and illustrated in figure 2(a), where collapse indicates spanwise homogeneity. The flow for $s/\delta \approx 0.39$ behaves as in the spatially uniform regime that shows a statistically homogeneous region, where, above the blending height, all the local defects collapse onto the reference spatially uniform shear stress defect. In this regime, the globally averaged defect trivially collapses onto the uniform shear stress defect, and the flow dynamically does not 'feel' the small spacings of the lateral stress variations. For intermediate spacings $s/\delta \approx 0.79, 1.57$ (figure 4c, e), outer-layer homogeneity is broken and the flow no longer behaves in the spatially uniform regime. No clear similarity structure of the local defects can be concluded from these plots but the local defects average to a flatter profile compared to the reference uniform shear stress defect. For the large spacings, $s/\delta \approx 3.14, 6.28$ (figure 4g, i), the local defects group into two depending on whether the y stations are in the high shear stress or low shear stress regions. Despite the scatter of the local defects, the globally averaged defect (figure 3) remarkably approaches the reference uniform shear stress defect; this will be further explored in §3.3.

The grouping of local defects into two indicates a tendency towards the spatially varying regime. As discussed in § 1.3 and illustrated in figure 2(b), the spatially varying regime can be measured by the local defect's collapse to the form according to (1.5). That is, the local defects, scaled with the local friction velocity, $u_{\tau H}$ or $u_{\tau L}$, collapse onto the functional form $f(z/\delta)$ that is identical to the spatially uniform regime (1.3). The right panels of figure 4 show the local defects scaled with the local friction velocity. As the spacing is increased, the tendency towards collapse according to (1.5) is unequivocal. At the largest spacing $s/\delta \approx 6.28$ (figure 4j), almost all the local defects collapse, except for a few y stations that are near a stress jump because the influence of the neighbouring patch cannot be ignored, a behaviour anticipated in figure 2(b). These plots corroborate the physical picture that the flow above a uniform shear stress patch in the spatially varying regime is not aware of the dynamics in neighbouring patches of a different shear stress provided the patch is wide enough.

3.3. *Global mean velocity defect of the spatially varying regime*

To understand why the global defect appears to approach the uniform shear stress defect in the spatially varying regime ($s \gg \delta$), consider the limiting case where each uniform stress patch is so large (s_H, $s_L \gg \delta$) that flow is dominated by local similarity in the sense of (1.5). In this limit, the flow regions near stress jumps make negligible contributions to the global average. Thus, we can relate the local defects to the global

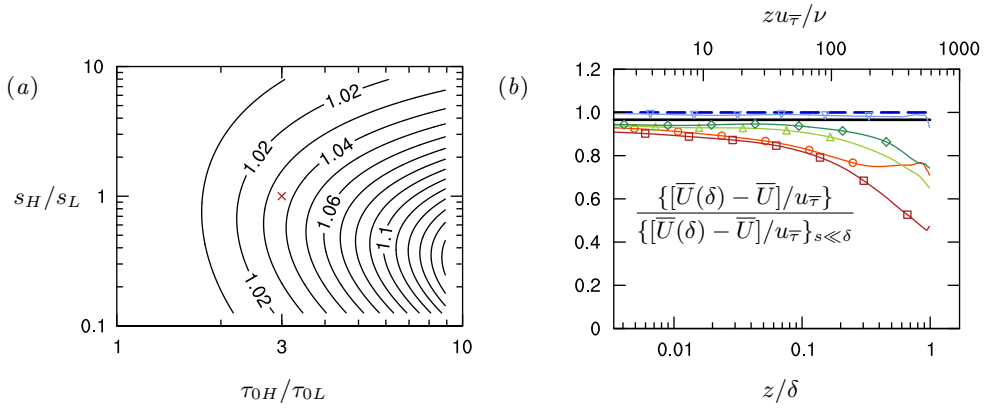

FIGURE 5. (*a*) Contours of gain factor, $G = (u_\tau)_{s\gg\delta}/(u_\tau)_{s\ll\delta}$, see (3.3*b*). The cross indicates the conditions of the present simulations ($\tau_{0H}/\tau_{0L} = 3$, $s_H/s_L = 1$), where $G \approx 1.035$. (*b*) Ratio of defect relative to spatially uniform limit: ——, $s \gg \delta$ limit, presently $1/G \approx 0.966$; – –, $s \ll \delta$ or uniform stress limit; —▽—, $s/\delta = 0.39$; —○—, $s/\delta = 0.79$; —□—, $s/\delta = 1.57$; —△—, $s/\delta = 3.14$; —◇—, $s/\delta = 6.28$.

defect via the wall-area-weighted average (cf. Mason 1988; Bou-Zeid *et al.* 2004),

$$\overline{U} \sim \frac{s_L}{s_L+s_H}U_L + \frac{s_H}{s_L+s_H}U_H, \quad \frac{\overline{\tau}_0}{\rho} \sim \frac{s_L}{s_L+s_H}\frac{\tau_{0L}}{\rho} + \frac{s_H}{s_L+s_H}\frac{\tau_{0H}}{\rho}. \quad (3.1a,b)$$

These are first rewritten, (3.1*a*) in defect form and (3.1*b*) in terms of friction velocities recalling the definitions, $u_{\overline{\tau}} \equiv (\overline{\tau}_0/\rho)^{1/2}$, $u_{\tau H} \equiv (\tau_{0H}/\rho)^{1/2}$ and $u_{\tau L} \equiv (\tau_{0L}/\rho)^{1/2}$:

$$\overline{U}(\delta) - \overline{U}(z) \sim \frac{s_L}{s_L+s_H}[U_L(\delta) - U_L(z)] + \frac{s_H}{s_L+s_H}[U_H(\delta) - U_H(z)], \quad (3.2a)$$

$$u_{\overline{\tau}}^2 \sim \frac{s_L}{s_L+s_H}u_{\tau L}^2 + \frac{s_H}{s_L+s_H}u_{\tau H}^2. \quad (3.2b)$$

We showed in figure 4 that outer-layer similarity is recovered locally when $s \gg \delta$, including in the wake. This result is supported by dimensional considerations emulating Townsend's leading to (1.5), as the local relative flow only sees the local friction velocity, the flow thickness and the outer-flow channel geometry, that is, the same conditions as for homogeneous channel flow. Thus, substituting the local similarity forms (1.5) into (3.2*a*), dividing by the square root of (3.2*b*) and rearranging, we obtain

$$\frac{\overline{U}(\delta) - \overline{U}(z)}{u_{\overline{\tau}}/G\left(\frac{\tau_{0H}}{\tau_{0L}}, \frac{s_H}{s_L}\right)} \sim f\left(\frac{z}{\delta}\right), \quad \text{where} \quad G = \frac{\left(1+\frac{s_H}{s_L}\right)^{1/2}\left(1+\frac{s_H}{s_L}\frac{\tau_{0H}}{\tau_{0L}}\right)^{1/2}}{1+\frac{s_H}{s_L}\left(\frac{\tau_{0H}}{\tau_{0L}}\right)^{1/2}}. \quad (3.3a,b)$$

G may be interpreted as a gain factor. That is, comparing (3.3) and (1.3), the global defect of the spatially varying regime obeys the same functional form as the global defect of the spatially uniform regime provided a gain G, the ratio of the friction velocity at large spacings relative to that at small spacings, i.e. $G = (u_{\overline{\tau}})_{s\gg\delta}/(u_{\overline{\tau}})_{s\ll\delta}$, is applied to the global-averaged friction velocity. Figure 5(*a*) plots the contours of G from (3.3*b*), showing that, under the conditions of the present simulations, i.e. $\tau_{0H}/\tau_{0L} = 3$ and $s_H/s_L = 1$, $G \approx 1.035$. In other words, the global velocity defect profile for large s/δ, after multiplying by 1.035, should approach the global velocity defect profile for small s/δ. This behaviour appears to be the case for $s/\delta \approx 6.28$ (figure 4*i*), comparing the global average (circled) line and the reference uniform shear stress (solid) line. This explains the

peculiar behaviour of why the global average defect of the spatially varying regime seems to approach the global defect of the spatially uniform regime. The present calculations suggest that the two are only expected to collapse to within a gain factor G, but G is near unity under the present conditions.

A more sensitive diagnostic is to consider the ratio of the normalised global defect relative to the normalised spatially uniform limit (figure 5*b*). In this plot, it can be clearly seen that the $s/\delta \approx 0.39$ defect behaves like the spatially uniform reference case and that the approach to the spatially varying regime by $s/\delta \approx 3.14$, 6.28 is clear, although even $s/\delta \approx 6.28$ is not large enough according to this diagnostic. Importantly, the defect of the intermediate spacings, $s/\delta \approx 0.79$, 1.57 undershoot the spatially varying regime, meaning that the changes from the spatially uniform to the spatially varying regime are not a mere interpolation between the two limiting behaviours. The undershoots imply a flatter profile in the bulk relative to the two limiting behaviours.

3.4. *Change in global skin-friction coefficient*

Before discussing the changes to the global skin-friction coefficient as observed in the present simulations, consider first the limit for large spacings of the global mean velocity profile relative to the wall $\overline{U}(z) - \overline{U}(0)$. To obtain this, let us assume that the flow obeys the law-of-the-wall similarity in a local sense when s/δ is large (figure 2*b*). Specifically, a local composite profile comprising the log law and a wake holds over each patch:

$$\frac{U_H(z) - U_H(0)}{u_{\tau H}} = \frac{1}{\kappa}\log\frac{z}{z_{0H}} + \frac{\Pi}{\kappa}w(z/\delta) \tag{3.4a}$$

$$\frac{U_L(z) - U_L(0)}{u_{\tau L}} = \frac{1}{\kappa}\log\frac{z}{z_{0L}} + \frac{\Pi}{\kappa}w(z/\delta) \tag{3.4b}$$

where $w(z/\delta)$ is Coles' wake function, and z_{0H} and z_{0L} are, respectively, the roughness lengths of the high and low shear stress regions. The roughness length is used without loss of generality. For a fully rough wall, the roughness length can be expressed in terms of the equivalent sand-grain roughness via $z_0 = k_s \mathrm{e}^{-\kappa(8.5)} \approx 0.033k_s$, for a no-slip smooth wall, the roughness length can be expressed in terms of the wall unit via $z_0 = (\nu/u_\tau)\mathrm{e}^{-\kappa A} \approx 0.13(\nu/u_\tau)$, and for the present (viscous) uniform shear-stress boundary condition, the roughness length can be expressed via $z_0 = (\nu/u_\tau)\mathrm{e}^{-\kappa(A-\Delta U^+)} \approx 0.50(\nu/u_\tau)$ as $\Delta U^+ \approx 3.4$ (Chung *et al.* 2014). Repeating the wall-area-weighted average similar to (3.1) for $\overline{U}(z) - \overline{U}(0)$, we obtain

$$\frac{\overline{U}(z) - \overline{U}(0)}{u_{\overline{\tau}}/G(\frac{\tau_{0H}}{\tau_{0L}}, \frac{s_H}{s_L})} \sim \frac{1}{\kappa}\log\frac{z}{z_{\overline{0}}} + \frac{\Pi}{\kappa}w(z/\delta), \tag{3.5}$$

where G is as before in (3.3*b*) and the effective roughness length is a harmonic average of the two,

$$z_{\overline{0}} = z_{0H}^{s_H u_{\tau H}/(s_H u_{\tau H} + s_L u_{\tau L})} z_{0L}^{s_L u_{\tau L}/(s_H u_{\tau H} + s_L u_{\tau L})}. \tag{3.6}$$

Presently, $z_{\overline{0}} \approx 0.50\nu/u_{\overline{\tau}}$, where $z_{0H} \approx 0.50\nu/u_{\tau H}$, $z_{0L} \approx 0.50\nu/u_{\tau L}$, $\tau_{0H}/\tau_{0L} = 3$ and $s_H/s_L = 1$ have been used. That is, there is negligible shift in the mean profile relative to the wall in the large-s/δ limit compared to the small-s/δ limit, although this may not be the case for other combinations of wall type, τ_{0H}/τ_{0L} and s_H/s_L. There is also negligible gain $G \approx 1.035$ in the slope of the log law (3.5). The change between the large-s/δ profile

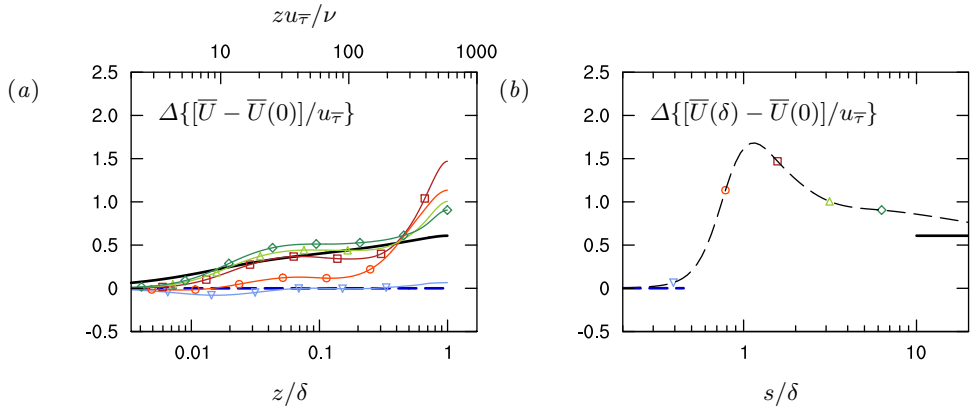

FIGURE 6. Change, relative to the uniform shear stress flow, of (a) global mean profile and (b) global skin-friction coefficient based on centreline velocity: ——, $s \gg \delta$ limit; – –, $s \ll \delta$ or uniform stress limit; —▽—, $s/\delta = 0.39$; —○—, $s/\delta = 0.79$; —□—, $s/\delta = 1.57$; —△—, $s/\delta = 3.14$; —◇—, $s/\delta = 6.28$.

and the small-s/δ profile is

$$\begin{aligned}\Delta\{[\overline{U}-\overline{U}(0)]/u_\tau\} &\equiv \{[\overline{U}-\overline{U}(0)]/u_\tau\}_{s\ll\delta} - \{[\overline{U}-\overline{U}(0)]/u_\tau\}_{s\gg\delta} \\ &\approx \Big(1-\frac{1}{G}\Big)\Big(\frac{1}{\kappa}\log\frac{z}{z_0}+\frac{\Pi}{\kappa}w(z/\delta)\Big) \\ &\approx \Big(1-\frac{1}{G}\Big)\{[\overline{U}-\overline{U}(0)]/u_\tau\}_{s\ll\delta}, \end{aligned} \tag{3.7}$$

where the approximation $z_{\overline{0}} \approx z_0$, has been used.

Figure 6(a) shows this change in global (spanwise-averaged) mean profile relative to the wall, along with the $s \ll \delta$ and $s \gg \delta$ limits, the former is zero by definition and the latter is obtained from (3.7). The approach to the large-s/δ limit does not appear to be monotonic, but a now familiar pattern emerges. For $s/\delta \lesssim 0.39$ or the spatially uniform regime, the mean profile remains mostly unchanged, and for $s/\delta \gtrsim 3.14$, the spatially varying regime is gradually approached, with even $s/\delta \approx 6.28$ not quite recovering the $s/\delta \gg 1$ limit. In between the two regimes $0.79 \lesssim s/\delta \lesssim 1.57$, there is an overshoot of $\Delta\{[\overline{U}-\overline{U}(0)]/u_\tau\}$ in the range $0.4 < s/\delta < 1$, indicating that the normalised global mean velocity profile reaches a minimum relative to the spatially uniform regime. The value of $\Delta\{[\overline{U}-\overline{U}(0)]/u_\tau\}$ at $z = \delta$ is plotted in figure 6(b). Specifically, figure 6(b) shows $\{[\overline{U}(\delta)-\overline{U}(0)]/u_\tau\}_{s\ll\delta} - \{[\overline{U}(\delta)-\overline{U}(0)]/u_\tau\}$. If we define C_f based on the centreline velocity relative to the wall velocity, $\overline{U}(\delta)-\overline{U}(0)$, then this quantity is simply $\sqrt{2/C_f}|_{s\ll\delta} - \sqrt{2/C_f}$. That is, a peak indicates an amplified skin-friction coefficient relative to the homogeneous case. The absolute of C_f is not meant to be related to any realistic values in this study, as it is highly sensitive to the near-wall treatment, i.e. the method of imposing stress variations. Of interest here is modifications to the relative motions in the outer layer. As such, a change, relative to the homogeneous case is the appropriate quantity here. This quantity can be linked to the fractional change in the skin-friction coefficient for a given s/δ relative to the skin-friction coefficient for $s \ll \delta$,

$$\begin{aligned}\frac{C_f - C_f|_{s\ll\delta}}{C_f|_{s\ll\delta}} &= \frac{1}{\big(1-\frac{\Delta\{[\overline{U}(\delta)-\overline{U}(0)]/u_\tau\}}{(2/C_f|_{s\ll\delta})^{1/2}}\big)^2} - 1 \\ &\approx (2C_f|_{s\ll\delta})^{1/2}\Delta\{[\overline{U}(\delta)-\overline{U}(0)]/u_\tau\}, \end{aligned} \tag{3.8}$$

where the approximation is simply a truncated Taylor series (cf. Spalart & McLean 2011). Figure 6(b) shows that the fractional change in skin-friction coefficient peaks near $s/\delta \approx 1$, higher than values in both the spatially uniform and spatially varying regimes. The value of the fractional change in skin-friction coefficient depends on $C_f|_{s\ll\delta}$; in the present simulations where $(2/C_f|_{s\ll\delta})^{1/2} \approx 18.0$ (cf. Chung *et al.* 2014), C_f is 18.8% greater than that of the spatially uniform regime, using the peak value of $\Delta\{[\overline{U}(\delta) - \overline{U}(0)]/u_\tau\} \approx 1.7$. This suggests a practical rule of thumb: lateral length scales on the order of the outer-layer thickness δ should be avoided in situations where low drag is desired. Also, surfaces with lateral length scales $\lesssim 0.5\delta$ have similar drag to uniformly rough surfaces. These predictions are consistent with Medjnoun, Vanderwel & Ganapathisubramani (2018).

3.5. *Secondary flow*

The results and dimensional reasoning heretofore reveal that, for the spatially uniform regime, a statistically homogeneous region occurs above the blending height, and for the spatially varying regime, a statistically homogeneous region occurs away from the stress jump. In these homogeneous regions, the identical outer-layer similarity form $f(z/\delta)$ according to either (1.3) or (1.5) emerge with no mean secondary flow $V(y,z) = W(y,z) = 0$. Away from the homogeneous regions, i.e. near the stress jump and below the blending height, mean (xt-averaged) secondary flow must appear. Figures 7 and 8 show the structure of the secondary flow in the vicinity of a stress jump, superimposed on contours of longitudinal isovels. Figure 7 retains the physical scaling with unity aspect ratio, which is useful for observing the increasing scale of the induced flow patterns with increasing s/δ; however, this scaling is not so useful for a global perspective because the range of spacings s is large. For a complete perspective, figure 8 is provided where the horizontal axes are scaled with s. The full extent of the mean cross-plane flow over a full period of low and high shear stress region is here visible for all s/δ.

First focussing on the secondary flow, observe that it organises into a pair of counter-rotating roll motions with an upwelling region that occurs over the low stress region, independent of spacing s. This is consistent with the link discovered by Hinze (1967, 1973), who associate the region of low shear stress with a higher dissipation relative to production, and, in turn, to an upwelling secondary flow. The strength and coverage of the roll motion depends on the spacing of the lateral stress variation s. At the small spacing, $s/\delta \approx 0.39$, identified as belonging to the spatially uniform regime, the roll motion is confined near the wall below the blending height, leaving a bulk region that is virtually homogeneous. At the intermediate spacings $s/\delta \approx 0.79$, 1.57, the roll motion strengthens and occupies the whole cross section of the bulk flow (more noticeable for $s/\delta = 1.57$). The wall-normal velocity between the roll motions increases substantially in both magnitude and spatial occupancy over this range of s/δ (compare vector lengths at $y = y_L$ in figure 8 and figure 9a). The result of this induced wall-normal velocity is a more efficient wall-normal mixing of longitudinal momentum, leading to a flatter longitudinal velocity profile as seen in figure 3. This effect on the velocity profile is consistent with the experimental observation made by Vanderwel & Ganapathisubramani (2015). At large spacings, $s/\delta \approx 3.14$, 6.28, identified as approaching the spatially varying regime, it is observed that the wall-normal velocity induced by the roll motions weakens, leading to an eventual homogeneous region between the roll motions. The roll motions generally move away from the stress jump towards the low shear stress region and remains up to δ. This explains the behaviour seen earlier, in figure 4(j) for example, where the velocity defect over almost all of the high shear stress region collapses well for large s/δ, but the same is not true for the low shear stress region. There is notably different behaviour of the spanwise velocity compared with the wall-normal as the size of the spacing increases,

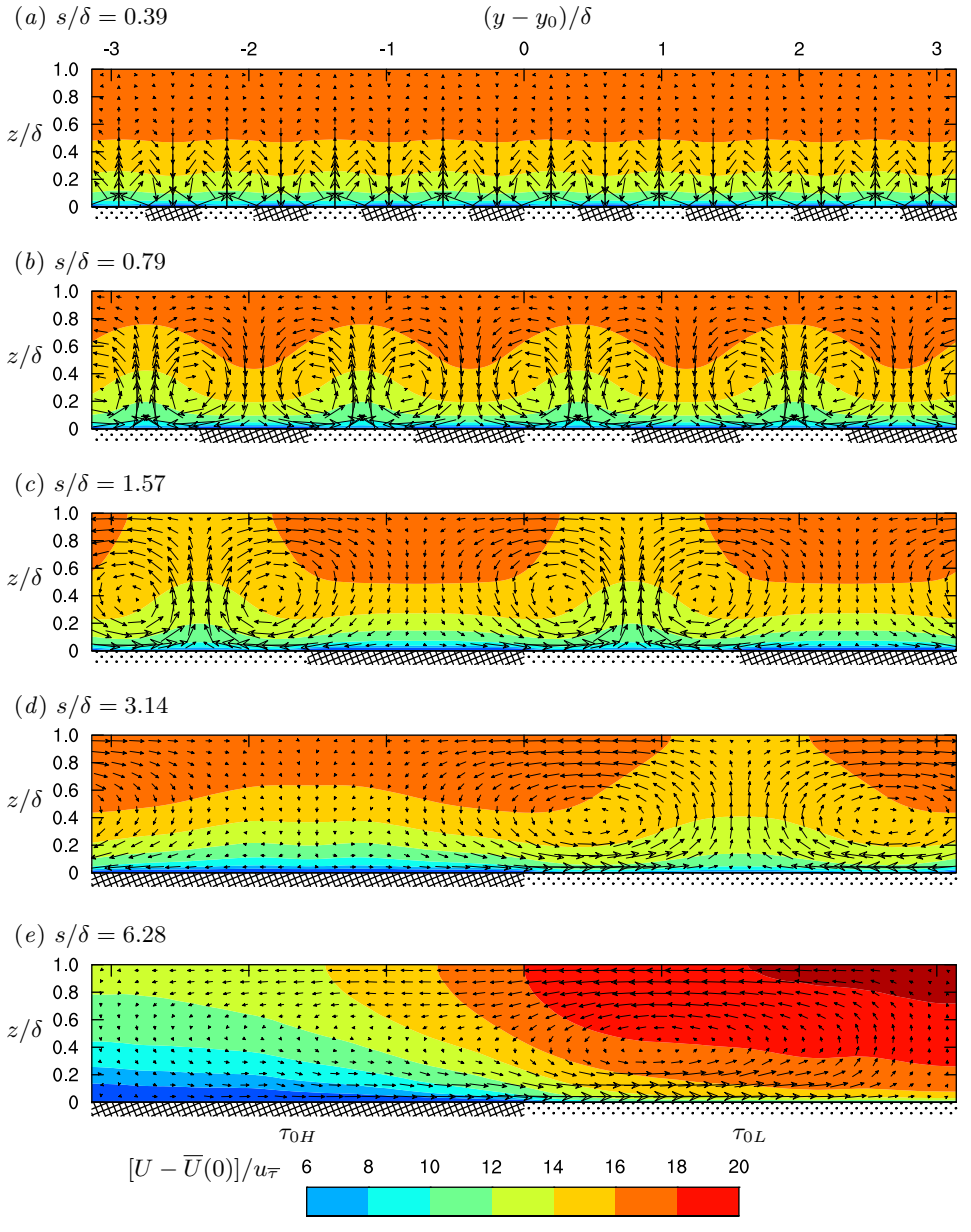

FIGURE 7. Mean (xt-averaged) longitudinal velocity U contours (isovels) in the cross (yz-) plane centred on high-to-low stress jump y_0. The (in-plane) secondary flow $[V - \overline{V}(0), W]/u_\tau$ is indicated by vectors, the lengths of which are scaled equally among the plots.

i.e. the maximum spanwise velocity in the plane is increasing monotonically with s/δ. This means there are two different roll motions depending on s/δ; in the classification of Bradshaw (1987): the roll motion for $s/\delta \lesssim 1.57$ is called 'Type (b)' or 'identifiable streamwise vortices', where $\partial V/\partial z$ is of the order of $\partial W/\partial y$, while the roll motion for $s/\delta \gtrsim 3.14$ is called 'Type (a)' or 'cross flow', where $\partial V/\partial z$ is far greater than $\partial W/\partial y$. It is the proximity of the counter-rotating roll motion pair that causes the behaviours seen in both W and V: when the roll motions are in close proximity ($s/\delta = 0.79, 1.57$), the

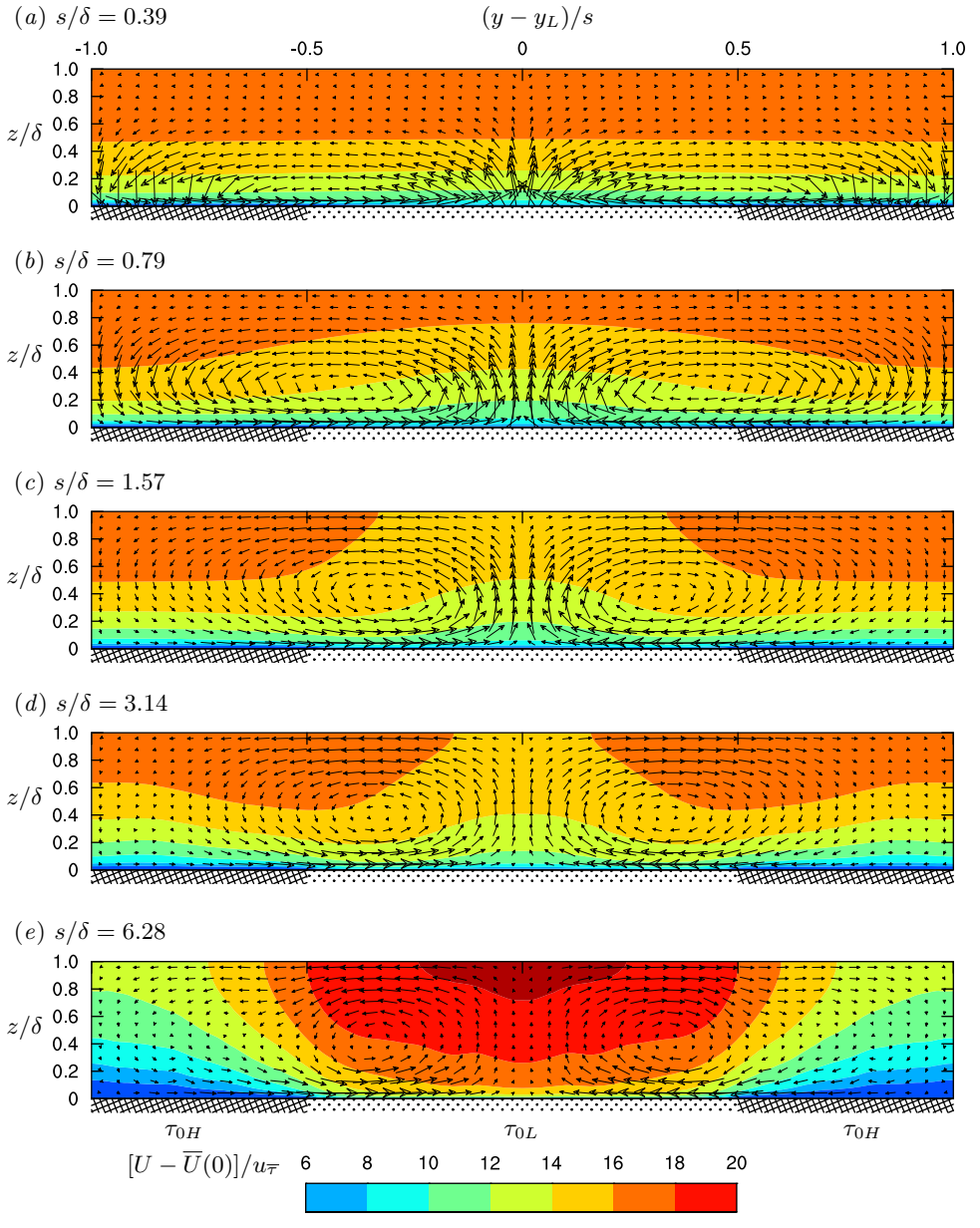

FIGURE 8. Mean (xt-averaged) longitudinal velocity U contours (isovels) in the cross (yz-) plane centred on low-shear-stress region y_L. Although there is always upwelling flow above the low shear stress region, the isovels show a sign reversal with increasing s/δ from low velocity over low shear stress for small s/δ to high velocity over low shear stress for large s/δ. The (in-plane) secondary flow $[V - \overline{V}(0), W]/u_\tau$ is indicated by vectors, the lengths of which are scaled equally among the plots.

wall-normal components add together, while the spanwise components counteract each other; when the roll motions are far apart, the wall-normal components freely decay and the spanwise components are enhanced by the wall without the influence of its pair.

Turning now to the longitudinal isovels, it can be observed in figure 8 that a reversal

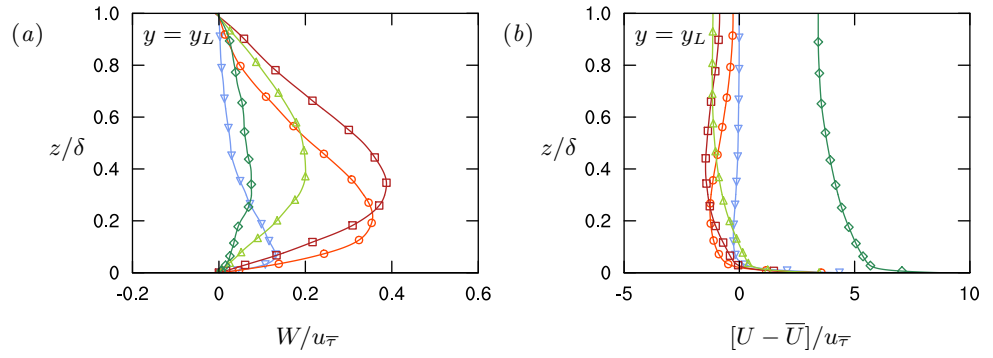

FIGURE 9. Wall-normal section profiles at the centre of the low-shear-stress region, $y = y_L$, of: (*a*) W/u_τ; (*b*) $[U - \overline{U}]/u_\tau$: ▽, $s/\delta = 0.39$; ○, $s/\delta = 0.79$; □, $s/\delta = 1.57$; △, $s/\delta = 3.14$; ◇, $s/\delta = 6.28$.

occurs near to the surface as s/δ increases. For low s/δ we observe low longitudinal velocity over the low shear stress region, but this switches for high s/δ with high longitudinal velocity over the low shear stress region. This is more evident in figure 9(*b*), where profiles of the local mean relative to the spanwise-averaged longitudinal velocity are shown at the centre of the low shear stress region. The possibility for either of these two configurations was first pointed out by Hinze (1973), but the conditions that favoured one over the other have not been addressed in the literature. Here, it is seen that the spatially varying regime ($s/\delta \gtrsim 6.28$) prefers the latter, a situation that is physically intuitive. If the flows over each region can be considered in isolation of neighbouring regions, it is expected that a higher longitudinal flow would be found over a low shear stress region owing to its lower resistance. However, for the small spacings $s/\delta \lesssim 3.14$, the flows over each region cannot ignore the presence of its neighbour and, a flow arrangement develops such that a large wall-normal velocity is produced over the low shear stress region (figure 9*a*). In any flow with shear in the wall-normal direction, the addition of a mean wall-normal velocity will transport low momentum from the wall and this is why a low longitudinal flow occurs over a low shear stress region as shown by Mehta & Bradshaw (1988). Indeed, such an arrangement of vortices has been reported, not only in laterally varying roughness studies (at spacings smaller than 3.14δ) such as Willingham *et al.* (2014), but also in smooth-wall, high Reynolds number wall-bounded flows, where conditional flow analyses have revealed natural high- and low-momentum regions that vary on the lateral spacing of order 0.5δ (e.g. Hutchins *et al.* 2011). The roll-motion structure is also reminiscent of that due to the linear non-normal growth mechanism (e.g. del Álamo & Jiménez 2006; Hwang & Cossu 2010). These similarities between the flow over laterally varying roughness at $s \lesssim 3.14\delta$ and smooth-wall studies suggest that the roughness variations act as a physical 'phase lock' that holds these linear-growth structures in space.

4. Conclusions

A numerical experiment to study the effects on wall turbulence of spanwise variations in wall shear stress is performed. Roughness effects are well known to depend on many parameters, which is the reason for limiting the varied parameters to the spanwise spacing of the high and low shear stress patches, s, and idealising the roughness heights and origins as prescribed uniform wall shear stresses. Although further studies could be performed with variation of parameters such as the ratio of wall shear stresses (τ_H/τ_L) or

the ratio of spacings (s_H/s_L), the current study provides sufficient insight to anticipate the effects of those parameters except, perhaps, in extreme cases.

The predominant effect of a sharp jump from high stress to low stress (in the spanwise direction) is the generation of streamwise roll motions. For small spacings, $s \lesssim 0.39\delta$, the roll motions produced are small and are confined so close to the wall that the flow behaves similarly (in the bulk) to a homogeneous rough or smooth wall flow. At very large spacings, i.e. $s \gtrsim 6.28\delta$, the roll motions and their induced velocities are confined to the stress jump such that the bulk of the flow over the high or low shear stress regions cares only about the local shear stress below it. Between these two limits, it is shown that there are some curious, perhaps counter-intuitive, behaviours in the secondary flow. It is between the spacings of $0.39 \lesssim s/\delta \lesssim 6.28$ that the roll motions become space filling and strongly interact with each other. This results in induced wall-normal velocities between the roll modes that first increase in magnitude with increasing s/δ, for $s/\delta \lesssim 1.57$, beyond which they decrease as s/δ further increases. It is this induced wall-normal velocity that is responsible for the noted counter-intuitive flow behaviours: a breakdown of outer-layer similarity, an increased drag over the expected mean and the previously unexplained switching between low and high longitudinal velocities over the low shear stress region.

This research was supported by resources provided by The Pawsey Supercomputing Centre with funding from the Australian Government and the Government of Western Australia and by the National Computing Infrastructure (NCI), which is supported by the Australian Government. This research was partially supported under the Australian Research Council's Discovery Projects funding scheme (project DP160103619).

Appendix A. Reynolds stresses in the cross plane

Although this paper is focussed on the similarity of mean quantities, we present in figure 10 four of the Reynolds stresses for the case $s/\delta \approx 0.79$. Similarity with the $S/\delta \approx 0.88$ case shown in figure 6(*a*, *b*, *c*, *d*) of Vanderwel & Ganapathisubramani (2015) is striking once upwelling regions are aligned. The upwelling regions correspond to low shear stresses in the present study and to the location of the protrusions in the study of Vanderwel & Ganapathisubramani (2015). The structure of these Reynolds stresses are also consistent with the $S/\delta \approx 3.14$ study of Anderson *et al.* (2015) seen in their figure 4(*a*, *c*, *k*, *g*), aligning their upwelling low-roughness regions with the present upwelling low shear stress regions. That τ_{zx} is more compact in the span than τ_{xx} is evident in all cases. Comparing Vanderwel & Ganapathisubramani (2015) and the present study, the relative magnitudes of Reynolds stresses are also similar, with maximum magnitudes indicated by maximum contour levels chosen to have identical relative ratios, $|\tau_{xx}|_{max} : |\tau_{zx}|_{max} : |\tau_{xy}|_{max} : |\tau_{yz}|_{max} \approx (10 : 2.5 : 2 : 1) \times 10^{-3} = 2.8 : 0.7 : 0.56 : 0.28$. The difference in absolute magnitudes is due to choice of scaling, U_∞^2 in Vanderwel & Ganapathisubramani (2015) and $\overline{\tau}_0$ presently. The ratio of maximum contour magnitudes in Anderson *et al.* (2015) is $8 : 1.2 : 0.5 : 0.05$, also similar, noting that their lower maximum contour magnitude for τ_{yz} provide more contrast in their figure 4(*g*). Despite the differences between the three flows, boundary layer over protrusions at $Re_\tau \approx 4200$ (Vanderwel & Ganapathisubramani 2015), open channel flow over wall-modelled roughness strips at atmospheric Reynolds numbers (Anderson *et al.* 2015) and channel flow over imposed stress variations at $Re_\tau \approx 590$ presently, the overwhelming similarities suggest that the present boundary conditions are effective at modelling the essence of secondary flows in the outer region.

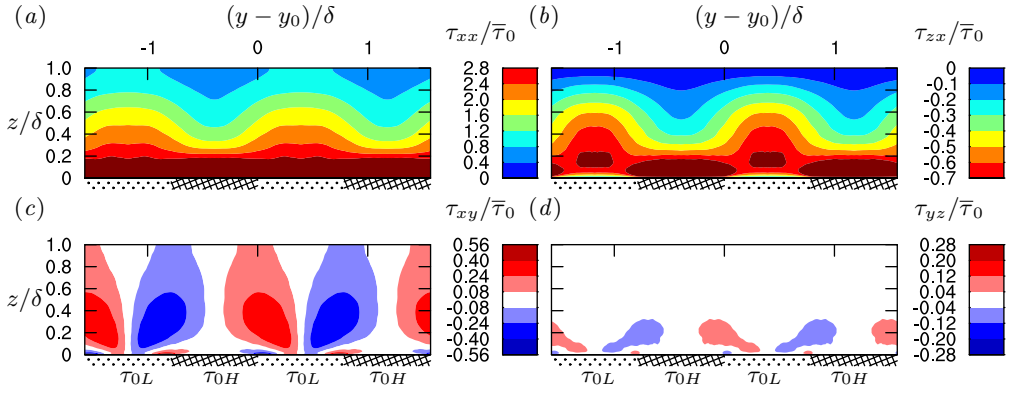

FIGURE 10. Reynolds stresses for the case $s/\delta \approx 0.79$ in the cross (yz-) plane: (a) $\tau_{xx} \equiv \rho\overline{u'u'}$, ($b$) $\tau_{zx} \equiv \rho\overline{w'u'}$, ($c$) $\tau_{xy} \equiv \rho\overline{u'v'}$ and (d) $\tau_{yz} \equiv \rho\overline{v'w'}$, where u', v' and w' are fluctuations.

REFERENCES

DEL ÁLAMO, J. C. & JIMÉNEZ, J. 2006 Linear energy amplification in turbulent channels. *J. Fluid Mech.* **559**, 205–213.

ANDERSON, W., BARROS, J. M., CHRISTENSEN, K. T. & AWASTHI, A. 2015 Numerical and experimental study of mechanisms responsible for turbulent secondary flows in boundary layer flows over spanwise heterogeneous roughness. *J. Fluid Mech.* **768**, 316–347.

ANTONIA, R. A. & LUXTON, R. E. 1971 The response of a turbulent boundary layer to a step change in surface roughness. Part 1. Smooth to rough. *J. Fluid Mech.* **48**, 721–761.

ANTONIA, R. A. & LUXTON, R. E. 1972 The response of a turbulent boundary layer to a step change in surface roughness. Part 2. Rough-to-smooth. *J. Fluid Mech.* **53**, 737–757.

BARROS, J. M. & CHRISTENSEN, K. T. 2014 Observations of turbulent secondary flows in a rough-wall boundary layer. *J. Fluid Mech.* **748**, R1.

BERNARDINI, M., PIROZZOLI, S., QUADRIO, M. & ORLANDI, P. 2013 Turbulent channel flow simulations in a convecting reference frames. *J. Comput. Phys.* **232**, 1–6.

BOU-ZEID, E., MENEVEAU, C. & PARLANGE, M. B. 2004 Large-eddy simulation of neutral atmospheric boundary layer flow over heterogeneous surfaces: blending height and effective surface roughness. *Water Resour. Res.* **40**, W02505.

BOU-ZEID, E., PARLANGE, M. B. & MENEVEAU, C. 2007 On the parameterization of surface roughness at regional scales. *J. Atmos. Sci.* **64**, 216–227.

BRADSHAW, P. 1987 Turbulent secondary flows. *Annu. Rev. Fluid Mech.* **19**, 53–74.

CHUNG, D., MONTY, J. P. & OOI, A. 2014 An idealised assessment of Townsend's outer-layer similarity hypothesis for wall turbulence. *J. Fluid Mech.* **742**, R3.

FLACK, K. A. & SCHULTZ, M. P. 2014 Roughness effects on wall-bounded turbulent flows. *Phys. Fluids* **26**, 101305.

FLACK, K. A., SCHULTZ, M. P. & CONNELLY, J. S. 2007 Examination of a critical roughness height for outer layer similarity. *Phys. Fluids* **19**, 095104.

GOLDSTEIN, D. B. & TUAN, T.-C. 1998 Secondary flow induced by riblets. *J. Fluid Mech.* **363**, 115–151.

HANSON, R. E. & GANAPATHISUBRAMANI, B. 2016 Development of turbulent boundary layers past a step change in wall roughness. *J. Fluid Mech.* **795**, 494–523.

HINZE, J. O. 1967 Secondary currents in wall turbulence. *Phys. Fluids* **10**, S122–S125.

HINZE, J. O. 1973 Experimental investigation on secondary currents in the turbulent flow through a straight conduit. *Appl. Sci. Res.* **28**, 453–465.

HUTCHINS, N., MONTY, J. P., GANAPATHISUBRAMANI, B., NG, H. C. H. & MARUSIC, I. 2011 Three-dimensional conditional structure of a high-Reynolds-number turbulent boundary layer. *J. Fluid Mech.* **673**, 255–285.

HWANG, Y. & COSSU, C. 2010 Linear non-normal energy amplification of harmonic and stochastic forcing in turbulent channel flow. *J. Fluid Mech.* **664**, 51–73.

Jelly, T. O., Jung, S. Y. & Zaki, T. A. 2014 Turbulence and skin friction modification in channel flow with streamwise-aligned superhydrophobic surface texture. *Phys. Fluids* **26**, 095102.

Jiménez, J. 2004 Turbulent flows over rough walls. *Annu. Rev. Fluid Mech.* **36**, 173–196.

Kozul, M., Chung, D. & Monty, J. P. 2016 Direct numerical simulation of the incompressible temporally developing turbulent boundary layer. *J. Fluid Mech.* **796**, 437–472.

Lozano-Durán, A. & Jiménez, J. 2014 Effect of computational domain on direct simulations of turbulent channels up to $Re_\tau = 4200$. *Phys. Fluids* **26**, 011702.

Mason, P. J. 1988 The formation of areally-averaged roughness lengths. *Q. J. R. Meteorol. Soc.* **114**, 399–420.

Medjnoun, T., Vanderwel, C. & Ganapathisubramani, B. 2018 Characteristics of turbulent boundary layers over smooth surfaces with spanwise heterogeneities. *J. Fluid Mech.* **838**, 516–543.

Mehta, R. D. & Bradshaw, P. 1988 Longitudinal vortices imbedded in turbulent boundary layers Part 2. Vortex pair with 'common flow' upwards. *J. Fluid Mech.* **188**, 529–546.

Moody, L. F. 1944 Friction factors for pipe flow. *Trans. ASME* **66**, 671–684.

Moser, R. D., Kim, J. & Mansour, N. N. 1999 Direct numerical simulation of turbulent channel flow up to $Re_\tau = 590$. *Phys. Fluids* **11**, 943–945.

Nugroho, B., Hutchins, N. & Monty, J. P. 2013 Large-scale spanwise periodicity in a turbulent boundary layer induced by highly ordered and directional surface roughness. *Int. J. Heat Fluid Flow* **41**, 90–102.

Perot, J. B. 1993 An analysis of the fractional step method. *J. Comput. Phys.* **108**, 51–58.

Raupach, M. R., Antonia, R. A. & Rajagopalan, S. 1991 Rough-wall turbulent boundary layers. *Appl. Mech. Rev.* **44**, 1–25.

Saito, N. & Pullin, D. I. 2014 Large eddy simulation of smooth-rough-smooth transitions in turbulent channel flows. *Int. J. Heat Mass Trans.* **78**, 707–720.

Sanderse, B., Verstappen, R. W. C. P. & Koren, B. 2014 Boundary treatment for fourth-order staggered mesh discretizations of the incompressible Navier–Stokes equations. *J. Comput. Phys.* **257**, 1472–1505.

Spalart, P. R. & McLean, J. D. 2011 Drag reduction: enticing turbulence, and then an industry. *Phil. Trans. R. Soc.* A **369**, 1556–1569.

Spalart, P. R., Moser, R. D. & Rogers, M. M. 1991 Spectral methods for the Navier–Stokes equations with one infinite and two periodic directions. *J. Comput. Phys.* **96**, 297–324.

Tennekes, H. & Lumley, J. L. 1972 *A first course in turbulence*. M. I. T. Press.

Townsend, A. A. 1976 *The structure of turbulent shear flow*, 2nd edn. Cambridge University Press.

Vanderwel, C. & Ganapathisubramani, B. 2015 Effects of spanwise spacing on large-scale secondary flows in rough-wall turbulent boundary layers. *J. Fluid Mech.* **774**, R2.

Verstappen, R. W. C. P. & Veldman, A. E. P. 2003 Symmetry-preserving discretization of turbulent flow. *J. Comput. Phys.* **187**, 343–368.

Willingham, D., Anderson, W., Christensen, K. T. & Barros, J. M. 2014 Turbulent boundary layer flow over transverse aerodynamic roughness transitions: induced mixing and flow characterization. *Phys. Fluids* **26**, 025111.